

Available online at [www.sciencedirect.com](http://www.sciencedirect.com)
**SciVerse ScienceDirect**
journal homepage: [www.elsevier.com/locate/jmbbm](http://www.elsevier.com/locate/jmbbm)

## Research paper

# Effect of high-energy X-ray doses on bone elastic properties and residual strains

A. Singhal<sup>a,\*</sup>, Alix C. Deymier-Black<sup>a</sup>, J.D. Almer<sup>b</sup>, D.C. Dunand<sup>a</sup>

<sup>a</sup> Department of Materials Science and Engineering, 2220 Campus Drive, Northwestern University, Evanston, IL 60208, USA

<sup>b</sup> Advanced Photon Source, Building 431, Argonne National Laboratory, 9700 S. Cass Avenue, Argonne, IL 60439, USA

### ARTICLE INFO

#### Article history:

Received 21 March 2011

Received in revised form

17 May 2011

Accepted 28 May 2011

Published online 21 June 2011

#### Keywords:

Irradiation

X-rays

Apparent modulus

Residual strain

Interface

### ABSTRACT

Bone X-ray irradiation occurs during medical treatments, sterilization of allografts, space travel and *in vitro* studies. High doses are known to affect the post-yield properties of bone, but their effect on the bone elastic properties is unclear. The effect of such doses on the mineral–organic interface has also not been adequately addressed. Here, the evolution of elastic properties and residual strains with increasing synchrotron X-ray dose (5–3880 kGy) is examined on bovine cortical bone. It is found that these doses affect neither the degree of nanometer-level load transfer between the hydroxyapatite (HAP) platelets and the collagen up to stresses of –60 MPa nor the microscopic modulus of collagen fibrils (both measured by synchrotron X-ray scattering during repeated *in situ* loading and unloading). However, the residual elastic strains in the HAP phase decrease markedly with increased irradiation, indicating damage at the HAP–collagen interface. The HAP residual strain also decreases after repeated loading/unloading cycles. These observations can be explained by temporary de-bonding at the HAP/collagen interface (thus reducing the residual strain), followed by rapid re-bonding (so that load transfer capability is not affected).

© 2011 Elsevier Ltd. All rights reserved.

## 1. Introduction

Biological tissues like bone and teeth are commonly exposed to a range of doses from X-rays, gamma and electron radiation during medical treatments, terminal sterilization and space travel. As an example, ionizing radiation is applied to the human body for the treatment of tumors around the head and neck region (Franzel and Gerlach, 2009; Kolovou and Anastassopoulou, 2007). During such treatments, in addition to targeting the tumor cells, the surrounding healthy cells are also affected, exposing the underlying bones and teeth to the applied doses which are of the order of 70 Gy (Engelmeier

and King, 1983; Franzel and Gerlach, 2009). Radiation doses of 25–35 kGy are commonly used for sterilizing bone allografts which are obtained from tissue banks or donors, to prevent transmission of infection (Akkus and Rimnac, 2001; Balsly et al., 2008; Currey et al., 1997; Kolovou and Anastassopoulou, 2007; McAllister et al., 2007; Salehpour et al., 1995; Simonian et al., 1994; Vastel et al., 2004; Zhang et al., 1994; Zioupos et al., 1999). Restorative dental materials, made using extracted teeth also need to be sterilized by radiation to minimize the risk of blood-borne pathogens (Brauer et al., 2008; Franzel and Gerlach, 2009; Moscovich et al., 1999; White et al., 1994). Also of great interest is the increasing use of synchrotron X-rays to determine the structure and mechanical properties

\* Corresponding author. Tel.: +1 847 467 5416, +1 773 290 9094 (Mobile); fax: +1 847 491 7820.

E-mail addresses: [AnjaliSinghal2007@u.northwestern.edu](mailto:AnjaliSinghal2007@u.northwestern.edu), [Anjali.singhal@gmail.com](mailto:Anjali.singhal@gmail.com) (A. Singhal).

1751-6161/\$ - see front matter © 2011 Elsevier Ltd. All rights reserved.

doi:10.1016/j.jmbbm.2011.05.035

of these biological materials (Barth et al., 2010; Deymier-Black et al., 2010), where doses in the range of 0.1–1 kGy/s are absorbed depending on the X-ray beam characteristics. Multiple measurements on the sample over long durations of time then result in accumulation of significantly large radiation doses on the sample. Additionally, astronauts on current deep space missions are exposed to radiation doses ranging from 0.2 to 2 Gy (depending on the amount and type of shielding used), due to galactic cosmic radiation and solar particle events which include protons, neutrons, heavy ions and gamma rays (Parsons and Townsend, 2000; Townsend, 2005; Townsend et al., 1992). Ionizing radiation from the various above sources can have deleterious effects on the mechanical properties, e.g., fracture toughness, bending strength and impact energy, of these hard tissues (Akkus and Rimnac, 2001; Currey et al., 1997; Franzel and Gerlach, 2009; Kolovou and Anastassopoulou, 2007; Salehpour et al., 1995), and, since they are often located in areas which experience mechanical loading, it is important to understand the severity of the effect of irradiation on the mechanical behavior of these tissues.

The dose-dependent response of bone and teeth, and its consequent effects on their mechanical properties, remain controversial. Most previous studies agree that the macroscopic elastic properties of the tissues, measured by three-point bend tests, remain unchanged with radiation doses up to 630 kGy (Barth et al., 2010; Currey et al., 1997) because they are primarily controlled by the properties of the mineral phase which is less susceptible to radiation damage. References (Franzel and Gerlach, 2009; Salehpour et al., 1995; Vastel et al., 2004), by contrast, showed degradation of bulk modulus and hardness in mineralized tissues for radiation doses up to 30 kGy, as measured by ultrasonic, tension–compression tests, and nano-indentation. The post-yield behaviors of bone and teeth have been found to be more affected by irradiation (Barth et al., 2010; Bowes and Moss, 1962), which is not surprising as this behavior is governed primarily by the mechanical integrity of the more susceptible collagen. According to the above studies, damage in the collagen fibrils, in the presence of water, takes place in the form of increased cross-linking due to free radicals produced by the radiolysis of water, or, in the absence of water, mostly by the cleavage of peptide chains occurring in the collagen backbone which makes up the basic structure of bone and teeth. However, there is little knowledge about the effect of irradiation on the interfacial interaction between the mineral (hydroxyapatite) and organic (mostly type-I collagen) phases. Hubner et al. (2005) have determined, using Fourier Transform Infrared Spectroscopy techniques, that ionizing radiation causes decarboxylation of the collagen side chains (bound to the phosphate groups on the HAP surface via calcium ions) at doses as low as 15 Gy, thus resulting in a weaker interface. Also, most of the studies mentioned previously cannot be directly compared with one another because they have been performed on bones of widely different ages and species.

The aim of the present study is to understand the effect of high doses of hard X-rays on the elastic properties and residual strains in bovine cortical bone at the nanoscopic level, both with and without an applied stress. The elastic behavior at the nanoscopic level is assessed by measuring the

load transfer between HAP platelets and the protein matrix via *in situ* loading with high-energy X-ray scattering, a method which has been applied to study the elastic deformation of bone (Akhtar et al., 2007, 2011; Almer and Stock, 2005, 2007), antler (Akhtar et al., 2008) and teeth (Almer and Stock, 2010; Deymier-Black et al., 2010), but without systematically addressing the question of irradiation-induced damage.

## 2. Materials and methods

### 2.1. Sample preparation

Fresh bovine femurs of two healthy 18-month old Angus breed cows were obtained: the first animal from a local slaughterhouse (Wilmette, IL), and the second from Aurora Packing Company Inc. (North Aurora, IL). These femurs were immediately cleaned of bone marrow and any attached ligaments using scalpels. Rough cuts, perpendicular to the femur long-axis, were made about 8.5 cm apart with an autopsy saw (Stryker® 810 autopsy saw, Kalamazoo, MI, USA), to get two rough femur cylinders. The epiphyses of the femur were removed. These cylinders were then wrapped in gauze soaked in Phosphate Buffered Saline (PBS) and frozen at  $-20^{\circ}\text{C}$ . Prior to further cutting, one cylinder was removed from the freezer and thawed to room temperature. Parallel cuts were made perpendicular to the long-axis of the femur, 5.5 mm apart with a low-speed diamond wafering saw (Buehler, Lake Bluff, IL). The transverse cross-section thus obtained was further cut 4.5 and 3.5 mm apart to get samples with dimensions  $5(\pm 0.01) \times 4(\pm 0.01) \times 3(\pm 0.01)\text{mm}^3$ , where the 5 mm dimension is always along the long-axis of the femur. Samples LR1 and LR2 were taken from the same femur of the first animal, close to the mid-diaphysis region, from adjacent locations. Samples LR3 and LR4 were taken from the second animal, also from adjacent locations and close to the mid-diaphysis region, at the lateral side of the femur. Samples L1-2 and R1-3 were taken from the same femur as LR3 and LR4, with L1-2 being taken from a region closer to the mid-diaphysis of the femur at the medial side and samples R1-3 from adjacent locations at the lateral side of the femur.

All cutting operations were done in DI water to prevent drying of bone. The dimensions of the samples were measured with a point micrometer, and the weight was measured with a precision balance, each time taking 3–5 measurements. The apparent density of the samples was calculated from the above measurements. The cut samples were then stored in PBS and frozen ( $-20^{\circ}\text{C}$ ) until the time of the diffraction experiments (6–12 months).

### 2.2. Diffraction measurements

All diffraction experiments were performed at beamline 1-ID-C of the Advanced Photon Source (APS) at Argonne National Laboratory. The experimental setup at the beamline is shown in Fig. 1. The bone sample is placed on the bottom platen of the compression system which has been adapted with a temperature-controlled hydration rig. The rig is composed of a vinyl tube connected to a pump which circulates PBS through a water-containing temperature-controlled bath,

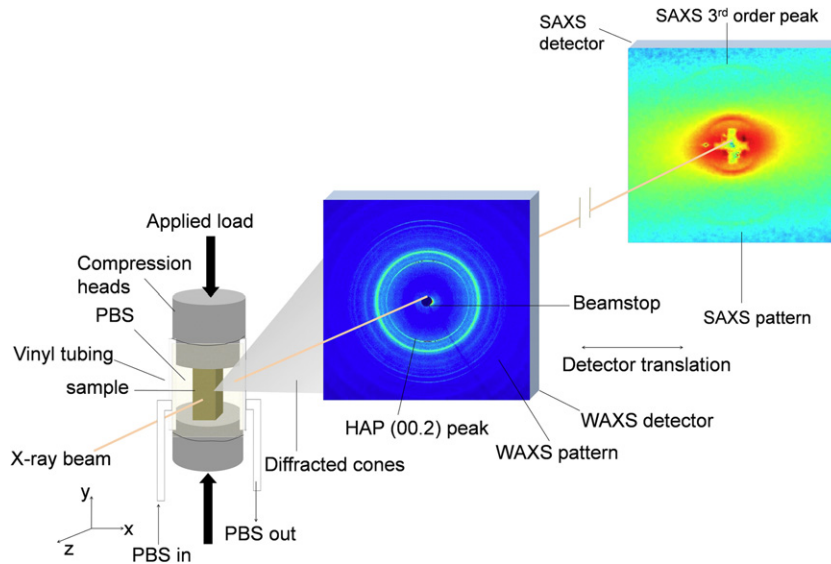


**Fig. 1 – Schematic of the X-ray diffraction measurement setup. The WAXS and SAXS patterns are shown with the (00.2) and third-order diffraction rings, respectively.**

thus maintaining the temperature of the PBS in which the sample is immersed. Preparatory experiments done using this setup showed that the temperature remains constant ( $\pm 0.7$  °C), as measured by a thermocouple, throughout the duration of the experiment. All tests were carried out at 37 °C, designated as body temperature, and the samples were loaded along the long-axis of the femur in compression.

#### 2.2.1. Load-unload and irradiation experiments

The samples were loaded in uniaxial compression between 0 and  $-60$  MPa in steps of  $-15$  MPa, taking diffraction measurements at each loading step with a  $50 \times 50 \mu\text{m}^2$  beam passing through the sample in a direction perpendicular to the loading axis (as shown in Fig. 1). The samples were loaded in the load-control mode where each loading step of  $-15$  MPa was carried out in 1 s; the samples were then unloaded in a single step in 1 s. The diffraction measurements (which involved data acquisition, detector read-out, and detector translation) at every load step took about 2 min. The applied stresses were slightly higher than the physiological stresses during rigorous activity (in the range of 20–40 MPa, as measured on sheep femurs and tibiae Lanyon and Baggott, 1976 and Rubin and Lanyon, 1984), because our goal was to investigate the damage mechanism in the limited amount of synchrotron beam time available. At the end of the load series, the sample was unloaded, and the cross-section of the beam was increased to  $4 \times 0.2 \text{ mm}^2$ , such that the entire width of the sample was exposed to the beam for a fixed time (which varied from 1.5 min to 2 h depending on the radiation dose applied). Due to the collimated undulator source, the intensity profile across the 4 mm width was not constant rather a Gaussian, with a full-width at half-maximum of approximately 2 mm such that the edges of the sample received approximately 3% of the flux at the center of the sample which is 4 mm wide. A tungsten plate was placed behind the sample during this wide-beam irradiation, to prevent scattered radiation from saturating the detector. This

process of load/unload irradiation was repeated ten times on sample LR1, nine times on sample LR2, and eight times on samples LR3-4. Samples LR1-2 (maximum accumulated dose of 1026 and 1947 kGy, respectively) were studied with 65 keV X-rays, and samples LR3-4 (both with maximum accumulated dose of 3840 kGy) with a 65.7 keV X-rays. The details of radiation exposure and load cycles are given for each sample in Table 1. The 1 s X-ray exposure time for each WAXS and SAXS measurement was sufficient to provide reasonable scattering statistics for the samples, and corresponds to doses of 0.54 and 0.73 kGy, within the irradiated volume, for samples LR1-2 and LR3-4, respectively. These absorbed doses were calculated from the X-ray flux and energy, the energy-dependent sample absorption, and the sample volume. Thus the absorbed dose for each load cycle, consisting of five diffraction measurements at stresses between 0 and  $-60$  MPa, is 2.7 and 3.7 kGy, respectively.

The Wide-Angle X-ray Scattering (WAXS) patterns were recorded by a GE-41RT flat panel detector ( $2048 \times 2048$  pixels,  $200 \mu\text{m}$  pixel size) which was placed at a distance of 1428 mm from the sample, and the Small-Angle X-ray Scattering (SAXS) patterns were recorded by a Princeton Instruments CCD ( $1000 \times 1000$  pixels,  $22.5 \mu\text{m}$  pixel size) placed at a distance of 4000 mm from the samples. A pressed ceria powder (NIST SRM 674-a) disc was used to calibrate the WAXS parameters at the beginning and end of experiments.

#### 2.2.2. Control experiments

Two sets of control experiments were performed with a 65 keV energy X-ray beam. In the first set of experiments, two samples (L1 and L2) were loaded from 0 to  $-60$  MPa in steps of  $-15$  MPa. The samples were unloaded to zero stress, held for 5 min and reloaded. This process was repeated eleven times (indicated in Table 1), every time taking WAXS and SAXS measurements at the same three locations,  $500 \mu\text{m}$  apart on the sample (horizontal center and one position each to the left and right), at every load, resulting in three stress-strain

**Table 1 – Chronological treatment of all samples, named according to their treatment routine, where L indicates load, R indicates irradiation, and LR a combination of load and irradiation.**

Irradiation and load/unload											
Sample	LR1										
Load cycles	1	2	3	4	5	6	7	8	9	10	11
Dose accumulated (kGy)	2.7	5.7	11.7	57.7	118.2	178.7	299.7	420.7	541.7	783.7	1025.7
Sample	LR2										
Load cycles	1	2	3	4	5	6	7	8	9	10	
Dose accumulated (kGy)	2.7	20.2	52.5	114.4	238.1	482.8	969.9	1941.4	1944.1	1946.8	
Sample	LR3										
Load cycles	1	2	3	4	5	6	7	8	9		
Dose accumulated (kGy)	3.7	68	193.1	439.5	928.8	1903.6	3849.7	3853.3	3857.0		
Sample	LR4										
Load cycles	1	2	3	4	5	6	7	8	9		
Dose accumulated (kGy)	3.7	68.2	193.3	439.7	929.0	1903.8	3849.9	3853.5	3857.2		
Load/unload only											
Sample	L1										
Load cycles	1	2	3	4	5	6	7	8	9	10	11
Sample	L2										
Load cycles	1	2	3	4	5	6	7	8	9	10	11
Irradiation only											
Sample	R1										
Dose accumulated (kGy)	1	46.6	137.9	320.4	685.4						
Sample	R2										
Dose accumulated (kGy)	1	45.5	134.5	312.6	668.7	1381.0	2805.5				
Sample	R3										
Dose accumulated (kGy)	1	46.7	138.0	320.6	685.8	1416.3	2877.3				

plots per sample. The samples were loaded in the load-control mode where each loading step of  $-15$  MPa was carried out in 1 s; the samples were then unloaded in a single step in 1 s. The diffraction measurements (which involved data acquisition, detector read-out, and detector translation) at every load step took about 2 min.

In the second set of control experiments, three samples (R1, R2 and R3) were irradiated to increasing doses with a  $4 \times 0.2$  mm<sup>2</sup> X-ray beam. A nominal load of  $-10$  N ( $\sim 0.85$  MPa) was maintained at all times to avoid motion in the sample during translation of the sample stage. At the beginning of the experiment and after every irradiation, diffraction measurements were made at the same three locations on the sample. These sample centers during wide-beam irradiation were horizontally off-centered by 1 mm relative to the beam center, whereas the diffraction measurements were done at the horizontal sample center and one location 500  $\mu$ m on either of its sides. The position 1 (leftmost measurement), thus received the least dose (9% of maximum) compared to position 2 ( $\sim 42\%$  of the maximum dose) and 3 ( $\sim 91\%$  of the maximum dose). Position 1 was then used as a internal control to guarantee that observed changes in internal strains were not caused by environmental effects such as dehydration or increased solution salination (Gustafson et al., 1996). After irradiation, the size of the X-ray beam was reduced back to  $50 \times 50$   $\mu$ m<sup>2</sup> for scattering measurements, under the same conditions described in Section 2.2.1. Sample R1 was irradiated to a maximum of 685 kGy while samples R2 and R3 were irradiated to a maximum of 2805 and 2877 kGy, respectively, as indicated in Table 1.

### 2.3. Diffraction analysis

The WAXS patterns are obtained from Bragg diffraction by the regularly spaced atomic planes of the crystalline HAP platelets. Longitudinal and transverse strains are determined from these patterns as previously discussed (Almer and Stock, 2005), and briefly summarized here. The diffraction pattern from ceria is first analyzed using the FIT2D software (Hammersley, 1998) to obtain the beam center, detector tilt and sample to detector distance. These parameters are then fed into a series of MATLAB programs which were developed at APS (Almer and Stock, 2005; Haeffner et al., 2005). The (00.2) diffraction ring is used to calculate the longitudinal and transverse strains, primarily because this ring is non-overlapping, and of relatively high intensity, thus reducing the error in peak measurements. Each diffraction pattern is read into the MATLAB program to calculate the radial position of the peak center (from the center of the pattern)  $R$ , as a function of azimuth  $\eta$ . These  $R$  vs.  $\eta$  plots for different stresses intersect at a single point  $R^*$ , corresponding to the point of invariant strain. This invariant point is then used to calculate the strains using the formula:

$$\varepsilon(\eta) = (R^* - R(\eta))/R(\eta). \tag{1}$$

The peak centers at  $\eta = 90 \pm 10$  and  $270 \pm 10^\circ$  are used to calculate the longitudinal strain, whereas those at  $\eta = 0 \pm 10$  and  $180 \pm 10^\circ$  are used to calculate the transverse strains (not reported here).

The contrast in SAXS patterns from mineralized tissues like bone primarily arises because of the difference in scattering from the high density HAP crystals, which are regularly arranged in the gap regions of the relatively less dense collagen

molecules. The measured change in SAXS spacing as a function of load is therefore the change in the average HAP platelet spacing, which in turn results from the cooperative deformation of the HAP and the collagen molecules. This gives the fibrillar strain (Gupta et al., 2006a). The centers of the third-order peak are determined, following a similar procedure to the WAXS patterns (Almer and Stock, 2007). The textured nature of the mineralized fibrils results in incomplete diffraction rings and fits are obtained only over  $90 \pm 10$  and  $270 \pm 10^\circ$ . Thus the strain-free point  $R^*$  cannot be determined as for WAXS, and the SAXS spacing at zero load is used as a reference to calculate the strains as a function of applied load.

The HAP and fibrillar strains are plotted as a function of the bulk applied stress. The slope of this graph is defined as the HAP ( $\sigma_{\text{applied}}/\varepsilon_{\text{HAP}}$ ) and fibrillar apparent modulus ( $\sigma_{\text{applied}}/\varepsilon_{\text{Fibril}}$ ), respectively. The change in apparent moduli and residual strains of HAP and fibrils as a function of the radiation dose is discussed in the following in the light of micromechanics of the composite structure of bone.

### 2.4. Ultrasonic modulus measurements

The macroscopic modulus of the samples was measured (after X-ray diffraction measurements) using an ultrasonic speed of sound technique, used previously to determine the elastic properties of bone (Lang, 1970). The ultrasonic velocities were determined by measuring the time of flight (TOF) of the ultrasonic pulses through bone samples of known thickness along the long-axis of the femur, using 5 MHz transducers (Matec Instruments, Northborough, MA), in the longitudinal and shear modes. The samples were mechanically coupled with a high viscosity fluid (molasses) to the transducers. The Matec software (MUIS-32) was used to create a pulse (SR9000) and record the output of the second transducer in through measurements. Three TOF measurements were made in longitudinal and shear modes in each of the samples along the axial direction of bone. The longitudinal and shear velocities,  $V_l$  and  $V_s$ , were used to calculate Young's modulus  $E$  and Poisson's ratio  $\nu$  according to Henneke-II (1998):

$$V_l = \sqrt{\frac{E(1-\nu)}{\rho(1+\nu)(1-2\nu)}} \quad (2a)$$

$$V_s = \sqrt{\frac{E}{2\rho(1+\nu)}} \quad (2b)$$

where  $\rho$  is the bone density.

## 3. Results

### 3.1. Young's modulus measurements

Young's moduli measured ultrasonically are shown in Table 2 along with the densities of the individual samples that were used for calculation (Eqs. (2a)–(2b)). The errors on the moduli were obtained by propagation from the standard deviations between the three TOF measurements. The average value from all the samples is  $20.2 \pm 1.2$  GPa. The moduli do not change appreciably between the samples, and exhibit a variation of about 6%. Since Young's modulus has been

shown to be correlated with HAP volume fraction (Currey, 1984; Sansalone et al., 2010), this indicates that the samples have near constant HAP content.

### 3.2. Load–unload and irradiation experiment

The HAP and fibrillar apparent moduli for samples LR1–4 are shown in Fig. 2. An example of the slope calculation is shown in Fig. 2(a), where the best-fit linear slopes are obtained, maximizing the  $r^2$  value in each case. In all samples, the apparent moduli of HAP or collagen fibrils show no systematic change with the radiation dose, as indicated by the horizontal dashed line in the figure corresponding to the average value. The average HAP and fibrillar moduli ( $E_{\text{app}}^{\text{HAP}}$  and  $E_{\text{app}}^{\text{Fib}}$ ) are given in Table 1 for sample LR1 (11 measurements,  $n = 11$ ), LR2 ( $n = 8$ ), LR3 ( $n = 7$ ) and LR4 ( $n = 7$ ). The  $E_{\text{app}}^{\text{Fib}}$  correlates well with  $E$  ( $r = 0.65$ ) and is not statistically different from  $E$  ( $p = 0.05$ ). The fibrillar apparent moduli have larger errors than the HAP apparent moduli due to lower signal-to-noise ratios.

The evolution of the residual strains in the HAP with radiation dose is shown in Fig. 3, with strains expressed in microstrain units ( $1 \mu\varepsilon = 10^{-6}$ ). These residual strains are calculated from diffraction measurements taken at the beginning of every loading cycle at zero stress after the sample irradiation. The first measurement is taken before any load or irradiation dose has been applied to the sample. Fig. 3 shows that the residual HAP strains become less compressive with increasing levels of radiation dose for all samples. The initial residual HAP strain in samples LR1 and LR2 are approximately twice those in samples LR3 and LR4, and the sample pairs LR1–2 and LR3–4 show good reproducibility. In all of the samples, the magnitudes of the residual strains initially are constant or increase slightly with irradiation, before exhibiting a rapid decrease. The curves of residual strains for samples LR1 and LR2 decrease rapidly up to 200 kGy before they merge with the curves for samples LR3 and LR4 and continue to decrease at a lower rate. The inset in Fig. 3 shows an expanded view of the same data from samples LR1–4 up to 500 kGy, where the transition in slope can be clearly seen. The net change in HAP strains is 1075  $\mu\varepsilon$  up to 1025 kGy for sample LR1, 1130  $\mu\varepsilon$  up to 1946 kGy for sample LR2, and 404 and 571  $\mu\varepsilon$  up to 3849 kGy for samples LR3 and LR4, respectively.

A plot of the HAP residual strain for the same samples LR1–4 is also shown as a function of the number of loading cycles in Fig. 4(a). As in Fig. 3, curves for samples LR1 and LR2 start at higher strain value and drop faster than those for samples LR3 and LR4, but all curves merge at the fifth cycle, beyond which all strain slopes are similar and low. Fig. 4(b) shows the plot of the change in fibrillar residual strains, compared to the starting residual strain (which is assumed to be zero) as a function of the number of loading cycles for samples LR1–4. Short exposure times (1 s) and the diffuse nature of the SAXS peaks make the fibrillar data noisier than that reported in a previous work (Almer and Stock, 2007). The strains become more compressive with increasing radiation dose for samples LR1–3, while those for sample LR4 exhibit no change with cycles, within the significant error range.

### 3.3. Control experiment—load–unload without irradiation

Samples L1 and L2 were loaded and unloaded 11 times, to determine the effect of mechanical deformation alone on the

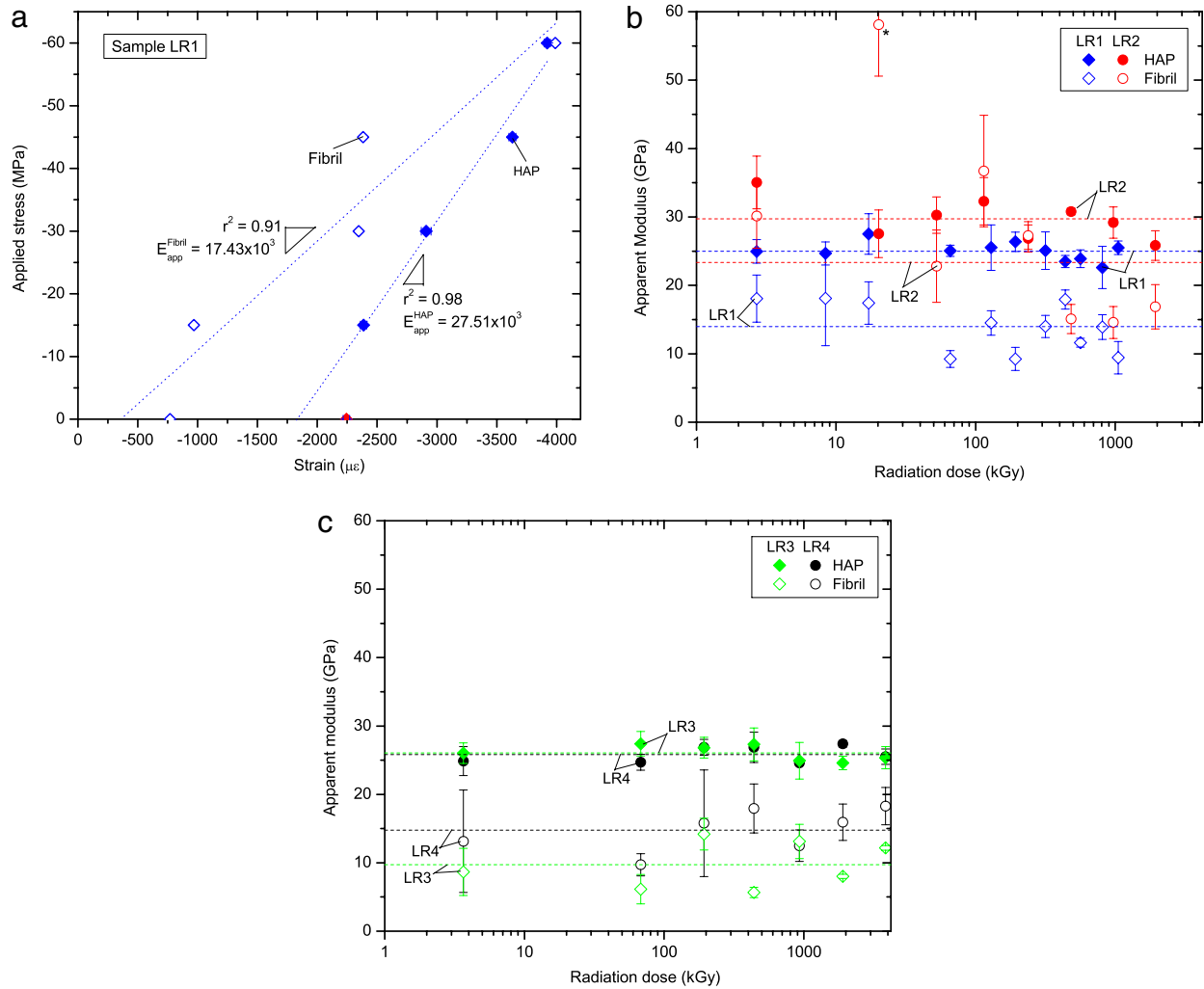


**Fig. 2 – (a) Plot of the HAP and fibrillar strains vs. applied stress showing a linear best-fit of the data for the third cycle of sample LR1. The data point marked in red has not been included in the slope calculation. (b) Plot of the apparent HAP and fibrillar moduli vs. radiation dose, for sample LR1-2 and (c) sample LR3-4. The dashed lines indicate the average value of the moduli for each sample. The data point indicated with an \* in figure (b) is an outlier that has not been included in the average. The error bars in figures (b) and (c) are the standard errors from least-squares fitting of the data, as shown in figure (a). (For interpretation of the references to colour in this figure legend, the reader is referred to the web version of this article.)**

**Table 2 – Density, Young’s modulus determined using ultrasonic measurements and apparent HAP and fibril modulus determined from X-ray scattering for each sample. The location of the sample within the cross-section of the femur is also indicated.**

Sample	Location	Density (g/cm <sup>3</sup> )	Young’s modulus (GPa)	Apparent HAP modulus (GPa)	Apparent Fibrillar modulus (GPa)
LR1	Anterior	2.10	19.5 ± 3.0	25.2 ± 1.3	13.7 ± 3.5
LR2	Posterior	2.09	21.5 ± 0.5	29.7 ± 3.0	23.4 ± 8.4
LR3	Posterior-lateral	2.04	19.7 ± 2.6	26.1 ± 1.2	9.71 ± 3.4
LR4	Posterior-lateral	2.05	21.4 ± 0.6	26.2 ± 1.2	14.8 ± 3.1
L1	Anterior-medial	2.06	22.1 ± 0.9	26.9 ± 1.7	18.3 ± 5.3
L2	Anterior-medial	2.07	20.8 ± 0.2	29.9 ± 2.0	21.1 ± 5.6
R1	Anterior-lateral	2.02	19.6 ± 0.5		
R2	Anterior-lateral	2.02	18.9 ± 2.0		
R3	Anterior-lateral	1.99	18.6 ± 0.5		

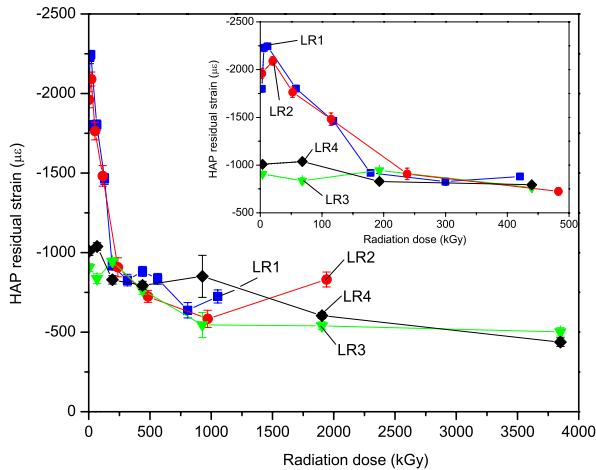


**Fig. 3** – Plot of HAP residual strain vs. radiation dose for samples LR1-4. The inset in the figure is an enlarged view of the data for these samples over the first 500 kGy. The error bars in these figures are the errors propagated from standard deviations of non-linear least-squares fitting of the diffraction peak centers.

residual strains and apparent modulus. As shown in Fig. 5(a), there is no systematic variation in the apparent modulus with loading cycles in both samples. The average  $E_{app}^{HAP}$  and  $E_{app}^{Fib}$  from samples L1 ( $n = 12$ ) and L2 ( $n = 12$ ) are given in Table 1.

The strains shown in Fig. 5(b) for each sample are averages of strains over the three locations at which measurements were done. The HAP residual strain decreases linearly with number of load cycles for these control samples with good reproducibility between samples L1 and L2. The net change in HAP strains is 310 and 550  $\mu\epsilon$ , respectively for samples L1 and L2, over 11 cycles. The fibrillar residual strains (data not shown here) exhibit a large scatter in their values between the three positions with no discernible trend and a net strain change over 11 cycles of 736 and  $-1106 \mu\epsilon$  for L1 and L2, respectively.

### 3.4. Control experiment—irradiation without load-unload

Samples R1-3 were irradiated without loading and unloading in order to determine the effect of irradiation alone on the residual strains. Sample R1 was subjected to a maximum dose of 685 kGy and samples R2 and R3 to a maximum dose of 2805 and 2877 kGy, respectively. Fig. 6(a) is a plot of the longitudinal residual HAP strain in samples R1-3 for position 3 (which received the maximum dose) as a function of the radiation dose. The figure also shows the residual strains at position 2 (which received 42% of the total dose), as a function of radiation dose, for these samples. These residual strains, at positions 2-3, decrease with increasing radiation dose. Fig. 6(b) shows the residual strains at each position 1, 2 and 3 in sample R3, plotted as a function of number of measurements. The residual strains at position 1 remain near constant within experimental error.

Fig. 6(a) also shows that the initial residual strain in samples R2 and R3 are about two times greater than that in sample R1. The magnitude of the residual strains in all the

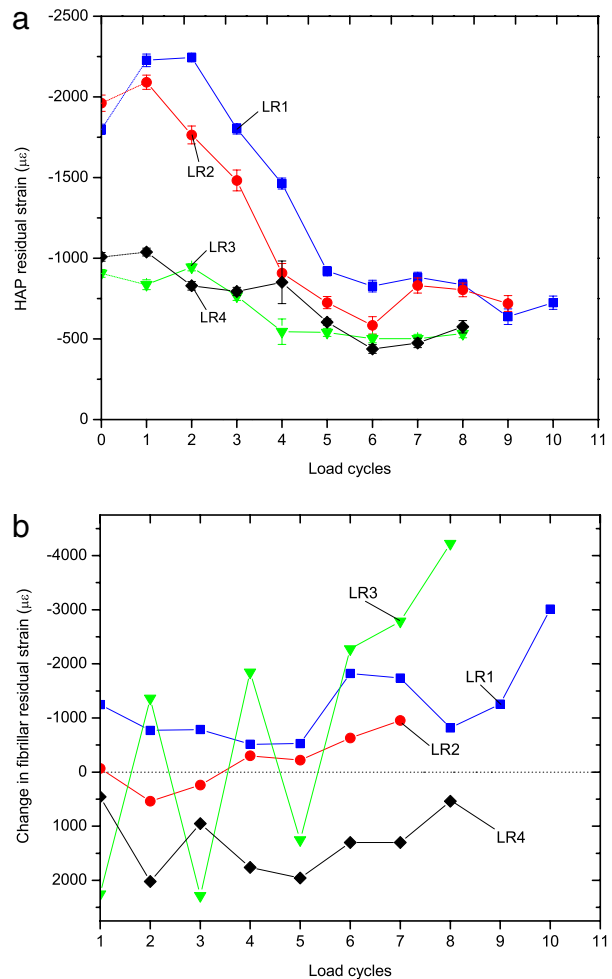


**Fig. 4** – Plot of (a) HAP residual strain (b) changes in fibrillar residual strain (compared to starting condition) vs. load-unload cycles for samples LR1-4. The error bars in figure (a) are the errors propagated from standard deviations of non-linear least-squares fitting of the diffraction peak centers.

samples decreases very rapidly after a dose of 47 kGy with a net change of 1478  $\mu\epsilon$  up to a dose of 685 kGy in sample R1, and 1570 and 920  $\mu\epsilon$  up to 2805 and 2877 kGy at position 3, in samples R2-3, respectively. The greatest change in strains takes place between 47 and about 300 kGy at both positions 2 and 3. The fibrillar strains for samples R1-3 have a large scatter with no discernible trend, resulting in much larger errors on their slope values and are thus not reported here.

## 4. Discussion

### 4.1. Apparent moduli

At the nanometer level, bone is made up of two materials, HAP and collagen, which have widely different elastic moduli. Load transfer is thus expected to occur between the two phases. The apparent modulus of HAP and fibrils is a measure of the extent of load transfer from the collagen matrix to the

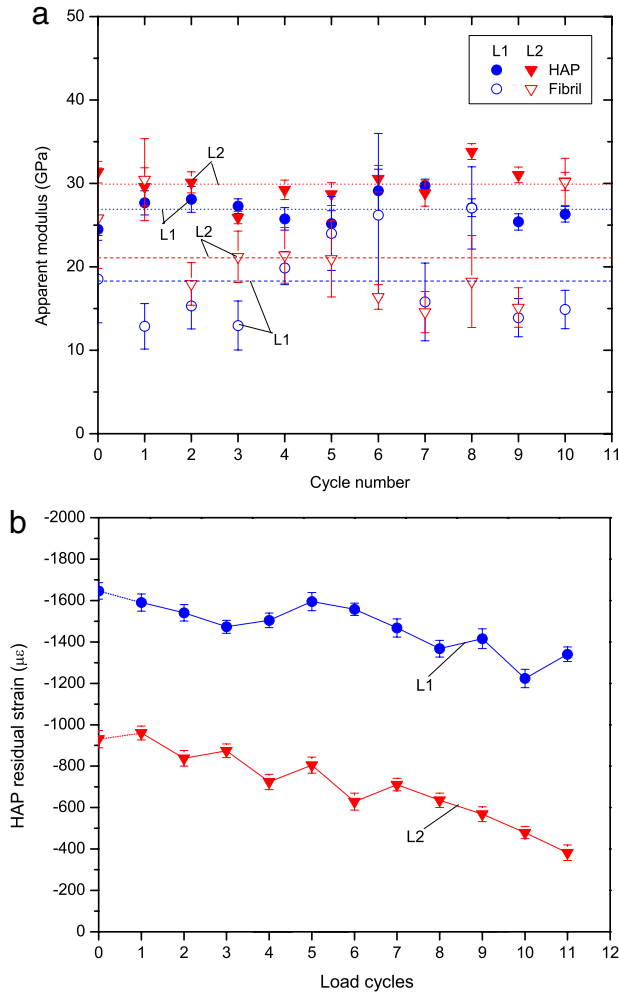


**Fig. 5 – (a) Plot of HAP and fibrillar moduli vs. load-unload cycles for samples L1-2. The dashed lines indicate the average value of each type of modulus in each sample. (b) Plot of HAP residual strain vs. load-unload cycles for samples L1-2. The data points in these figures at any cycle are the average of the measurements done at 3 different points on the sample. The error bars are propagated from the errors on the 3 individual moduli at any cycle, where the errors on individual moduli are standard errors obtained from least-squares fitting as shown in Fig. 2(a).**

HAP platelets (Deymier-Black et al., 2010; Yuan et al., 2010). The average  $E_{app}^{HAP}$  in the present experiments is  $27.3 \pm 2.0$  GPa measured from the (00.2) HAP reflection. Other studies done using X-ray diffraction have shown a lower value of  $18 \pm 2$  GPa for bovine dentin (Deymier-Black et al., 2010), a higher value of  $38 \pm 0.5$  GPa for canine fibula (Almer and Stock, 2007), and a close value of  $29.3 \pm 6.3$  GPa for bovine femur (Singhal et al., in preparation). However, biological materials are very heterogeneous from one location to another, with variations in the microstructure, distribution of the mineral phase and porosity (Meyers et al., 2008), thus a direct comparison between moduli of different species is difficult. Also, the experimental conditions such as temperature and hydration state at which the aforementioned tests were done are different. However, the fact to be noted is that  $E_{app}^{Fib}$

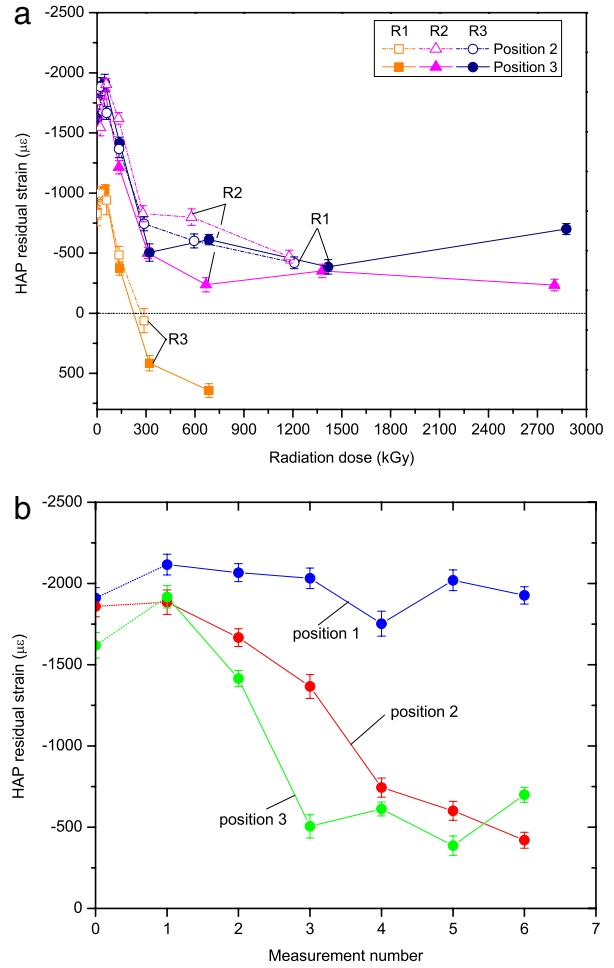


**Fig. 6 – (a) Plot of HAP residual strain vs. radiation dose for samples R1-3 at position 2 with hollow symbols and position 3 with solid symbols. (b) Plot of HAP residual strain vs. measurement number for sample R3 at three locations. Note position-dependent irradiation. The error bars in these figures are the errors propagated from standard deviations of non-linear least-squares fitting of the diffraction peak centers.**

( $16.8 \pm 4.6$  GPa) is much lower than  $E_{app}^{HAP}$  ( $27.3 \pm 2.0$  GPa). Given that HAP is much stiffer than collagen, a lower strain in HAP (respectively a higher strain in collagen) would be expected as compared to the HAP/collagen composite fibril. Since the apparent modulus is proportional to the inverse of the strain and the bulk applied stress is taken to be the same for both phases, the fact that the  $E_{app}^{Fib}$  is lower than the  $E_{app}^{HAP}$  is justified. The applied stress-phase strain curves of the two phases, shown in Fig. 2(a), are linear up to the maximum applied stress which was  $-60$  MPa (fibrillar strain of  $-4000 \mu\epsilon$ ) as would be expected for a compressive system. Thus the samples tested here do not exhibit a critical strain effect beyond which there is macroscopic yielding (at a fibrillar strain of  $2000 \mu\epsilon$ ) as seen by Hoo et al. (2011), where bone was tested under tensile loading. The greater strength of bone in compression further suggests that it is adapted to being predominantly loaded in compression (Reilly and Currey, 1999; Taylor et al., 1996).

The average value of  $E_{\text{app}}^{\text{Fib}}$  obtained here ( $16.8 \pm 5.1$  GPa) is close to the value from the previous experiments which report  $18.0 \pm 1.2$  GPa (Almer and Stock, 2007) on the canine fibula and  $18.2 \pm 1.1$  GPa on bovine femur (Singhal et al., in preparation). The heterogeneity in bone can be seen from the variation of  $E_{\text{app}}^{\text{HAP}}$  within a single bone sample which is, for example,  $\sim 15\%$  between the measurements at three different positions, separated by 0.5 mm from each other, on sample L1. The variation of  $E_{\text{app}}^{\text{Fib}}$  between measurements at different positions is much greater, e.g. 23% for sample L1.

The average value of Young's modulus determined by ultrasonic measurements is  $20.2 \pm 1.2$  GPa. This value is very close to that found in previous ultrasonic measurements, of 21.9 GPa on bovine femur (age, sex unknown) (Buskirk et al., 1981), and 20.7 GPa for human tibial bone (age, sex, cause of death unknown) (Rho et al., 1993) and reasonably close to values of  $27.6 \pm 1.7$  GPa and  $29.7 \pm 3.5$  GPa for fresh, unembalmed human and canine femora, respectively (age and sex unknown) (Ashman et al., 1984). The fibrillar strain represents the cooperative deformation between the HAP and collagen molecules (which make up the mineralized collagen fibril). Recalling from Section 2.3, the fibrillar strain arises from the change in the periodic spacing of the HAP crystals. This 'nano-scale composite' modulus ( $E_{\text{app}}^{\text{Fib}}$  is measured at the nano-scale by scattering over a micron-scale volume) is then related to the overall sample Young's modulus ( $E$  is measured over the whole sample volume by ultrasound), since bone is made up of an assembly of mineralized collagen fibrils, but without accounting for the larger scale structures like extra-fibrillar HAP, porosity, osteons, and lamellae. As expected, these moduli show similar average values ( $E_{\text{app}}^{\text{Fib}} = 16.8 \pm 5.1$  GPa and  $E = 20.8 \pm 1.0$  GPa at  $p = 0.05$  level) and a clear correlation is found between  $E_{\text{app}}^{\text{Fib}}$  and  $E$  for samples LR1-4 and L1-2 ( $R = 0.65$ ). The extra-fibrillar HAP is known to be present outside the collagen fibrils and will act as a reinforcement to the fibril; but its volume fraction has been the topic of considerable debate (Bonar et al., 1985; Katz and Li, 1973). This HAP would contribute to the WAXS strain, but not to the SAXS strain due to its lack of periodic arrangement similar to the intra-fibrillar HAP. The presence of the extra-fibrillar HAP could thus result in a higher Young's modulus compared to the fibrillar modulus.

The fact that  $E_{\text{app}}^{\text{HAP}}$  and  $E_{\text{app}}^{\text{Fib}}$  do not change significantly and systematically with increasing radiation doses in samples LR1-4 (Fig. 2) suggests that the degree of load transfer to HAP via shear from the collagen matrix (Gupta et al., 2006a, 2005, 2006b) remains unchanged at the radiation levels measured. A change in the  $E_{\text{app}}^{\text{HAP}}$  with dose would indicate greater or lesser elastic strains transferred to HAP via collagen, as observed e.g. in inorganic composites when interfacial de-bonding occurs (Daymond et al., 1999; Gupta et al., 2006b; Young et al., 2007).

Irradiation has been shown to cause radiolysis of the water present in the collagen fibrils which produces free radicals resulting in the formation of inter-molecular cross-links in the collagen structure, thereby increasing its stiffness (Brauer et al., 2008; Salehpour et al., 1995). Such changes would not be observable in the  $E_{\text{app}}^{\text{HAP}}$  or  $E_{\text{app}}^{\text{Fib}}$  values, because of the large difference between Young's moduli of the bulk phases of HAP (114 GPa) and collagen (1 GPa) (Grenoble

et al., 1972; Jager and Fratzl, 2000). Even doubling or tripling the modulus of collagen would not result in a significant change of the  $E_{\text{app}}^{\text{HAP}}$ . An estimate for the lower bound of the apparent modulus can be achieved by calculating  $E_{\text{app}}^{\text{HAP}}$  using a Voigt model similar to Ref. Deymier-Black et al. (2010) (upper bound for stress, and thus elastic strain, carried by HAP for a given composite strain), using average volume composition values of HAP (41%), collagen (38%) and water (21%) from Ref. Olszta et al. (2007). A value of 47 GPa was obtained (using the modulus of HAP and collagen as 114 and 1 GPa, respectively); doubling or tripling the modulus of collagen changes the calculated value of  $E_{\text{app}}^{\text{HAP}}$  only by 0.81 and 1.6%, respectively. The reason for a higher  $E_{\text{app}}$  in these calculations as compared to the experimental value has been attributed to the fact that Young's modulus of the HAP platelet must be lower than 114 GPa due to the combined effects of the nano-crystalline nature of HAP, carbonate substitution in HAP and surface adsorption, as discussed in detail in Ref. Deymier-Black et al. (2010). Also, the Voigt model is for continuous, aligned reinforcements, whereas the HAP platelets are discontinuous and not fully aligned with the applied load.

#### 4.2. Residual strains

The HAP residual strains are found to become less compressive (i.e., their magnitude decreases), and those in the collagen fibrils are in general found to become more compressive (magnitude increases) with increasing radiation and load cycles (Figs. 3–4). The increase in fibrillar residual strains can be explained by permanent "plastic" deformation of the collagen network which was not recovered during unloading. This unrecovered permanent compressive strain, causes a decrease in the SAXS spacing, and thus an increase in the fibrillar strains measured. The decrease in HAP residual strain indicates that, although the  $E_{\text{app}}^{\text{HAP}}$  is the same as discussed above, there is a net relaxation of the HAP crystals after every load-unload cycle. This could occur due to a de-bonding/re-bonding process during the repetitive loading/unloading and/or interfacial de-bonding due to accumulated radiation (Deymier-Black et al., in preparation).

##### 4.2.1. Effect of load-unload cycles

Initial residual strains are known to occur during the growth phase of the HAP crystals, and may serve to limit crack growth at low loads *in vivo* (Ascenzi and Benvenuti, 1977; Ascenzi, 1999; Goodyear et al., 2009). They have been found to be dependent to a large extent on the *in vivo* loading history of the region from which the bone samples were obtained (Giri et al., 2008; Todoh et al., 2000). The repetitive loading and unloading in the present experiments, much like a low cycle fatigue experiment, may be responsible for some of the decrease in HAP residual strains observed in Fig. 4(a). When the HAP-collagen composite is loaded, the collagen molecules deform by shear, transferring stress and strain to the HAP platelets (Gupta et al., 2006a, 2005, 2006b). Since, the interface between HAP and collagen consists of van der Waals and electrostatic types of interactions (Franzel and Gerlach, 2009; Thompson et al., 2001; Walsh and Guzelsu, 1994; Walsh

et al., 1994; Wise et al., 2007) which break and repair with relative ease, the high interfacial stresses developed during transfer of load can cause failure of some of the interfacial bonds. Glue proteins are also known to be present at the HAP–collagen interface, and mediate the interaction between HAP and collagen through water (Fantner et al., 2005; Wilson et al., 2006). These serve as sacrificial bonds and allow the material to maintain its interfacial strength. Breakage of bonds allows the HAP platelets to relax because the initial constraints placed on the platelets at the interface have been reduced. Upon subsequent unloading, some of the broken bonds between the matrix and the HAP platelets can reform, but in a different configuration than before due to the molecular sliding which took place during the deformation, thus providing a different level of constraint when the applied load reaches zero again.

#### 4.2.2. Effect of irradiation

Irradiation also affects HAP relaxation beyond the simple loading and unloading, as seen from Fig. 3. It has been found that when a human cortical bone sample is irradiated, interfacial de-bonding can occur at the HAP–collagen interface in the form of decarboxylation of the collagen side chains bound to the phosphate groups at the HAP surface (Hubner et al., 2005). With fewer interfacial bonds the interface can weaken more easily when load is applied, thus resulting in the relaxation of the HAP residual strains on unloading. In fact, this effect is so large that it can be measured at zero applied stress as well, as seen in Fig. 6(a). However, since the  $E_{app}^{HAP}$  and  $E_{app}^{Fib}$  do not change significantly and systematically with increasing doses or number of cycles, it can be inferred that the de-bonded or re-bonded condition of the interface at every  $E_{app}^{HAP}$  measurement is the same, or that this de-bonding level is not significant enough to reduce the rate at which load is transferred to the HAP phase when an external load is applied.

The evolution of residual strain in samples LR1 and LR2 are very similar to each other but quite different from that in samples LR3 and LR4. This could be due to the fact that samples LR1, LR2 and LR3, LR4 are obtained from femurs which belong to two different cows which may have slightly different properties. The initial residual HAP strains in samples LR1 and LR2 are twice those in samples LR3 and LR4. Also, lack of data for LR3 and LR4 between 2 and 64 kGy does not allow for any true comparisons between the initial shapes of these residual strain vs. radiation curves with those of LR1 and LR2. The ultrasonic moduli of the samples LR1-2 are not significantly different from samples LR3-4, L1-2 and R1-3 which were all obtained from the same bone of the same animal. However, the samples LR3, LR4, L2 and R1 have lower initial residual strain values than all the other samples indicating a location dependence of the initial residual strains in samples which were taken from the same bone of the same animal. Despite the aforementioned differences, the four samples LR1-4 show a similar pattern of decreasing residual strains with dose, with LR1 and LR2 being more rapid initially, and all four decreasing at the same rate after a dose of about 200 kGy.

#### 4.2.3. Proposed mechanism

To decouple the interfacial de-bonding caused due to loading/unloading and the radiation dose, control experiments were done as described in Section 2.2.2. The magnitude of the HAP residual strains decreases almost linearly with increasing number of measurement cycles in the control samples (L1-2) which were tested without additional irradiation. On the other hand, the strains decrease non-uniformly with increasing radiation doses on samples R1-3 which were irradiated without load–unload cycles. In this case, the residual strains decrease rapidly starting at a dose of 47 kGy (Fig. 6(a)). The constraints applied on the HAP by the surrounding collagen matrix resulting in compressive residual strains in the HAP, are relieved allowing the platelets to relax, with increasing dose and cycle. Also, Fig. 6(b) shows that the net change in strains in position 1 is negligible, as compared to positions 2 and 3. This would suggest that the relaxation of HAP in these samples is indeed a consequence of radiation or mechanical deformation, and not due to simply holding the sample in that specific environment for that period of time.

The linear shapes of the residual strains vs. loading cycles curves of samples L1 and L2 (Fig. 5(b)), replicate those of samples LR3 and LR4 but not samples LR1 and LR2 (Fig. 4(a)). On the other hand, the shapes of the residual strain vs. dose curves of samples R1-3 (Fig. 6(a)) replicate those of samples LR1-4 well (Fig. 3). The different rates of relaxation of these samples can be explained by their different initial residual strains. Higher initial residual strains in the HAP platelets provide a greater driving force for it to relax upon removal of some of the constraints, thus resulting in a faster relaxation. These higher initial residual strain samples (LR1, LR2, R2, R3) relax at a rate which is about an order of magnitude faster compared to the samples with a lower initial residual strain (LR3, LR4), taking into consideration only position 3 in samples R2 and R3. However, the residual strains from all these samples tend to converge toward  $-570 \mu\epsilon$  as seen from Figs. 3(a) and 6(a), despite the different initial residual strains on these samples, which could indicate that an equilibrium value of residual strain exists at that radiation dose level. Sample R1 is an exception to the lower initial residual strain case, which relaxes rapidly towards zero. This could arise because of sample variability. Additionally, higher level architecture has not been considered in our analyses, which also plays an important role in the mechanical behavior. For example, if the X-ray beam samples an array of Haversian canals aligned along the path of the beam, the strains would relax faster (because it has fewer HAP platelets which will bear the same load, resulting in greater compliance) compared to a case where the X-ray beam passes through lamellae.

To determine the dominant factor in the decrease of the residual strains in samples LR1-4 (Figs 3 and 4(a)), the two control experiments L1-2 (Fig. 5) and R1-3 (Fig. 6) can be compared. The average of the change (decrease) in residual strains in samples L1-2 is  $430 \mu\epsilon$  over 11 cycles. The average change in residual strains in the other set of control samples R2-3 (position 3 in each case) is  $1250 \mu\epsilon$  up to a dose of 2840 kGy, with most of the change occurring up to about 650 kGy. The net change in strains in these control samples can then be compared individually with those of samples

LR1-4 which were loaded-unloaded as well as irradiated, and decrease much more slowly at this radiation dose. As seen from Fig. 3 and Table 1, the sample LR1 has undergone 11 load-unload cycles after an irradiation dose of 1025 kGy, LR2, 8 cycles up to 1940 kGy, and LR3-4 only 6 load-unload cycles after 1903 kGy of radiation. If load-unload is assumed to be the primary cause of interfacial de-bonding, decrease in strains of 430  $\mu\epsilon$  would occur for LR1, 313  $\mu\epsilon$  for LR2 and 235  $\mu\epsilon$  for LR3-4. A comparison of the aforementioned values with that obtained if radiation was assumed to be the primary cause of the de-bonding (1250  $\mu\epsilon$ ) clearly suggests that the residual strains relax significantly more due to the radiation dose alone than due to repeated load-unload.

The pattern of decrease of the residual strains suggests that there is a critical dose level, between 20 and 60 kGy in these experiments, beyond which the HAP platelets relax upon further irradiation. Below this dose, significant property degradation from a weakening of the HAP-collagen interface is not measured. A similar radiation dose interval between 0.05 and 70 kGy was also found in an earlier study (Barth et al., 2010), above which post-yield plastic deformation disappeared. After the rapid decrease period (Figs. 3, 4(a), 6), the HAP platelets relax at a slower rate and tend to reach mechanical equilibrium with the surrounding collagen matrix, which is in a state of lower residual compression.

It can then be concluded from the above observations, that for samples LR1-4 the relaxation of the HAP platelets occurs due to interfacial de-bonding at the HAP-collagen interface, primarily because of the irradiation occurring between the load-unload cycles at these stress levels, and to a lesser extent from the mechanical cycles themselves.

## 5. Conclusions

The apparent moduli of HAP (which quantifies the extent of load transfer) and fibrils (which correlates to the sample strain) were measured at high radiation doses, on 18-month old bovine femur samples. The apparent moduli of HAP and the collagen fibrils remain unaffected up to the highest radiation dose of 3836 kGy used here.

The residual strain in HAP becomes less compressive with increasing radiation doses, whereas those in the fibrils became more compressive. The HAP residual strains decreased after a threshold radiation dose identified to be between 20 and 60 kGy. The former observation is interpreted as caused by interfacial de-bonding at the pre-strained HAP-collagen interface, due to both loading and irradiation. From the control experiments, it was determined that the relaxation of HAP platelets was primarily due to the de-bonding resulting from irradiating the samples, and, to a lower extent, by mechanical loading and unloading the samples.

## Acknowledgments

The authors thank Prof. L. Catherine Brinson (NU), Dr. Stuart Stock (NU) and Dr. Dean Haefner (APS) for numerous useful discussions throughout this work as well as Ms. Yu-chen

Karen Chen and Mr. Fang Yuan (NU) for their help with the experiments at the APS. This research was performed at station 1-ID of XOR-APS. Use of the Advanced Photon Source was supported by the US Department of Energy, Office of Science, Office of Basic Energy Sciences, under Contract No. DE-AC02-06CH11357.

## REFERENCES

- Akhtar, R., Daymond, M.R., Almer, J.D., Mummery, P.M., 2007. Load transfer in bovine plexiform bone determined by synchrotron X-ray diffraction. *Journal of Materials Research* 23.
- Akhtar, R., Daymond, M.R., Almer, J.D., Mummery, P.M., 2008. Elastic strains in antler trabecular bone determined by synchrotron X-ray diffraction. *Acta Biomaterialia* 4, 1677-1687.
- Akhtar, R., Daymond, M.R., Almer, J.D., Mummery, P.M., 2011. Lattice strains and load partitioning in bovine trabecular bone. *Acta Biomaterialia* 7, 716-723.
- Akkus, O., Rinnac, C.M., 2001. Fracture resistance of gamma radiation sterilized cortical bone allografts. *Journal of Orthopaedic Research* 19, 927-934.
- Almer, J.D., Stock, S.R., 2005. Internal strains and stresses measured in cortical bone via high-energy X-radiation. *Journal of Structural Biology* 152.
- Almer, J.D., Stock, S.R., 2007. Micromechanical responses of mineral and collagen phases in bone. *Journal of Structural Biology* 157.
- Almer, J.D., Stock, S.R., 2010. High energy X-ray scattering quantification of in situ-loading-related strain gradients spanning the dentin/enamel junction (DEJ) in bovine tooth specimens. *Journal of Biomechanics* 43, 2294-2300.
- Ascenzi, M.-G., 1999. A first estimation of prestress in so-called circularly fibered osteonic lamellae. *Journal of Biomechanics* 32, 935-942.
- Ascenzi, A., Benvenuti, A., 1977. Evidence of a state of initial stress in osteonic lamellae. *Journal of Biomechanics* 10, 447-453.
- Ashman, R.B., Cowin, S.C., Van Buskirk, W.C., Rice, J.C., 1984. A continuous wave technique for the measurement of the elastic properties of cortical bone. *Journal of Biomechanics* 17, 349-361.
- Balsly, C.R., Cotter, A.T., Williams, L.A., Gaskins, B.D., Moore, M.A., Wolfenbarger Jr., L., 2008. Effect of low dose and moderate dose gamma irradiation on the mechanical properties of bone and soft tissue allografts. *Cell and Tissue Banking* 9, 289-298.
- Barth, H.D., Launey, M.E., MacDowell, A.A., Ager, J.W., Ritchie, R.O., 2010. On the effect of X-ray irradiation on the deformation and fracture behavior of human cortical bone. *Bone* 46, 1475-1485.
- Bonar, L.C., Lees, S., Mook, H.A., 1985. Neutron diffraction studies of collagen in fully mineralized bone. *Journal of Molecular Biology* 181, 265-270.
- Bowes, J.H., Moss, J.A., 1962. The effect of gamma radiation on collagen. *Radiation Research* 16, 211-223.
- Brauer, D.S., Saeki, K., Hilton, J.F., Marshall, G.W., Marshall, S.J., 2008. Effect of sterilization by gamma radiation on nano-mechanical properties of teeth. *Dental Materials* 24, 1137-1140.
- Buskirk, W.C.V., Cowin, S.C., Ward, R.N., 1981. Ultrasonic measurement of orthotropic elastic constants of bovine femoral bone. *Journal of Biomechanical Engineering* 103.
- Currey, J.D., 1984. Effects of differences in mineralization on the mechanical properties of bone. *Philosophical Transactions of the Royal Society of London. Series B, Biological Sciences* 304.

- Currey, J.D., Foreman, J., Laketic, I., Mitchell, J., Pegg, D.E., Reilly, G.C., 1997. Effects of ionizing radiation on the mechanical properties of human bone. *Journal of Orthopaedic Research* 15, 111–117.
- Daymond, M.R., Lund, C., Bourke, M.A.M., Dunand, D.C., 1999. Elastic phase-strain distribution in a particulate-reinforced metal-matrix composite deforming by slip or creep. *Metallurgical and Materials Transactions A* 30A.
- Deymier-Black, A.C., Almer, J.D., Stock, S.R., Haeffner, D.R., Dunand, D.C., 2010. Synchrotron X-ray diffraction study of load partitioning during elastic deformation of bovine dentin. *Acta Biomaterialia* 6, 2172–2180.
- Deymier-Black, A., Yuan, F., Singhal, A., Almer, J.D., Dunand, D.C., Creep mechanisms in bone and dentin via high-energy X-ray diffraction (in preparation).
- Engelmeier, R.L., King, G.E., 1983. Complications of head and neck radiation therapy and their management. *The Journal of Prosthetic Dentistry* 49, 514–522.
- Fantner, G.E., Hassenkam, T., Kindt, J.H., Weaver, J.C., Birkedal, H., Pechenik, L., Curtoni, J.A., Cidade, G.G., Stucky, G.D., Morse, D.E., Hansma, P.K., 2005. Sacrificial bonds and hidden length dissipate energy as mineralized fibrils separate during bone fracture. *Nature Materials* 4, 612–616.
- Franzel, W., Gerlach, R., 2009. The irradiation action on human dental tissue by X-rays and electrons—a nanoindenter study. *Zeitschrift für Medizinische Physik* 19, 5–10.
- Giri, B., Tadano, S., Fujisaki, K., Todoh, M., 2008. Understanding site-specific residual strain and architecture in bovine cortical bone. *Journal of Biomechanics* 41, 3107–3115.
- Goodyear, S.R., Gibson, I.R., Skakle, J.M.S., Wells, R.P.K., Aspden, R.M., 2009. A comparison of cortical and trabecular bone from C57 black 6 mice using Raman spectroscopy. *Bone* 44, 899–907.
- Grenoble, D.E., Katz, J.L., Dunn, K.L., Gilmore, R.S., Murty, K.L., 1972. Elastic properties of hard tissues and apatites. *Journal of Biomedical Materials Research* 6.
- Gupta, H.S., Seto, J., Wagermaier, W., Zaslansky, P., Boescke, P., Fratzl, P., 2006a. Cooperative deformation of mineral and collagen in bone at the nanoscale. *Proceedings of the National Academy of Sciences* 103.
- Gupta, H.S., Wagermaier, W., Zickler, G.A., Aroush, D.R.-B., Funari, S.S., Roschger, P., Wagner, H.D., Fratzl, P., 2005. Nanoscale deformation mechanisms in bone. *Nano Letters* 5.
- Gupta, H.S., Wagermaier, W., Zickler, A., Hartmann, J., Funari, S.S., Roschger, P., Wagner, H.D., Fratzl, P., 2006b. Fibrillar level fracture in bone beyond the yield point. *International Journal of Fracture* 139.
- Gustafson, M.B., Martin, R.B., Gibson, V., Storms, D.H., Stover, S.M., Gibeling, J., Griffin, L., 1996. Calcium buffering is required to maintain bone stiffness in saline solution. *Journal of Biomechanics* 29, 1191–1194.
- Haeffner, D.R., Almer, J.D., Lienert, U., 2005. The use of high energy X-rays from the advanced photon source to study stresses in materials. *Materials Science and Engineering A* 399.
- Hammersley, A.P., 1998. FIT2D V9.129 reference manual V3.1 ESRF 98HA01T. ESRF External Report.
- Hoo, R.P., Fratzl, P., Daniels, J.E., Dunlop, J.W.C., Honkimäki, V., Hoffman, M., 2011. Cooperation of length scales and orientations in the deformation of bovine bone. *Acta Biomaterialia* 7, 2943–2951.
- Hubner, W., Blume, A., Pushnjakova, R., Dekhtyar, Y., Hein, H.-J., 2005. The influence of X-ray radiation on the mineral/organic matrix interaction of bone tissue: an FT-IR microscopic investigation. *The International Journal of Artificial Organs* 28, 66–73.
- Henneke-II, E.H., 1998. Ultrasonic testing. In: McIntire, P. (Ed.), *Non-Destructive Testing Handbook*. American Society for Non-Destructive Testing, pp. 36–58.
- Jager, I., Fratzl, P., 2000. Mineralized collagen fibrils: a mechanical model with a staggered arrangement of mineral particles. *Biophysical Journal* 79.
- Katz, E.P., Li, S.-T., 1973. Structure and function of bone collagen fibrils. *Journal of Molecular Biology* 80, 1–15.
- Kolovou, P., Anastassopoulou, J., 2007. Synchrotron FT-IR spectroscopy of human bones. The effect of aging. *Brilliant Light in Life and Material Sciences* 267–272.
- Lang, S.B., 1970. Ultrasonic method for measuring elastic coefficients of bone and results on fresh and dried bovine bones. *IEEE Transactions on Biomedical Engineering BME* 17.
- Lanyon, L., Baggott, D., 1976. Mechanical function as an influence on the structure and form of bone. *Journal of Bone and Joint Surgery* 58-B, 436–443.
- McAllister, D.R., Joyce, M.J., Mann, B.J., Vangsness Jr., C.T., 2007. Allograft update: the current status of tissue regulation, procurement, processing, and sterilization. *The American Journal of Sports Medicine* 35.
- Meyers, M.A., Chen, P.-Y., Lin, A.Y.-M., Seki, Y., 2008. Biological materials: structure and mechanical properties. *Progress in Materials Science* 53, 1–206.
- Moscovich, H., Creugers, N.H.J., Jansen, J.A., Wolke, J.G.C., 1999. In vitro dentine hardness following gamma-irradiation and freezing. *Journal of Dentistry* 27, 503–507.
- Olszta, M.J., Cheng, X., Jee, S.S., Kumar, R., Kim, Y.-Y., Kaufman, M.J., Douglas, E.P., Gower, L.B., 2007. Bone structure and formation: a new perspective. *Materials Science and Engineering R58*.
- Parsons, J.L., Townsend, L.W., 2000. Interplanetary crew dose rates for the August 1972 solar particle event. *Radiation Research* 153, 729–733.
- Reilly, G.C., Currey, J.D., 1999. The development of microcracking and failure in bone depends on the loading mode to which it is adapted. *The Journal of Experimental Biology* 202, 543–552.
- Rho, J.Y., Ashman, R.B., Turner, C.H., 1993. Young's modulus of trabecular and cortical bone material: ultrasonic and microtensile measurements. *Journal of Biomechanics* 26, 111–119.
- Rubin, C.T., Lanyon, L.E., 1984. Dynamic strain similarity in vertebrates; an alternative to allometric limb bone scaling. *Journal of Theoretical Biology* 107, 321–327.
- Salehpour, A., Butler, D.L., Proch, F.S., Schwartz, H.E., Feder, S.M., Doxey, C.M., Ratcliffe, A., 1995. Dose-dependent response of gamma irradiation on mechanical properties and related biochemical composition of goat bone-patellar tendon-bone allografts. *The Journal of Bone and Joint Surgery* 13, 898–906.
- Sansalone, V., Naili, S., Bousson, V., Bergot, C., Peyrin, F., Zarka, J., Laredo, J.D., Haiat, G., 2010. Determination of the heterogeneous anisotropic elastic properties of human femoral bone: from nanoscopic to organ scale. *Journal of Biomechanics* 43, 1857–1863.
- Simonian, P.T., Conrad, E.U., Chapman, J.R., Harrington, R.M., Chansky, H.A., 1994. Effect of sterilization and storage treatments on screw pullout strength in human allograft bone. *Clinical Orthopaedics and Related Research* 302, 290–296.
- Singhal, A., Almer, J.D., Dunand, D.C., (in preparation). Load partitioning between mineral and protein phases during compressive deformation of bone.
- Taylor, M.E., Tanner, K.E., Freeman, M.A.R., Yettram, A.L., 1996. Stress and strain distribution within the intact femur: compression or bending? *Medical Engineering & Physics* 18, 122–131.
- Thompson, J.B., Kindt, J.H., Drake, B., Hansma, H.G., Morse, D.E., Hansma, P.K., 2001. Bone indentation recovery time correlates with bond reforming time. *Nature Materials* 414, 773–776.

- Todoh, M., Tadano, S., Shibano, J.-i., Ukai, T., 2000. Polychromatic X-ray measurements of anisotropic residual stress in bovine femoral bone. *JSME International Journal Series C* 43.
- Townsend, L.W., 2005. Implications of the space radiation environment for human exploration in deep space. *Radiation Protection Dosimetry* 115, 44–50.
- Townsend, L.W., Wilson, J.W., Shinn, J.L., Curtis, S.B., et al., 1992. Human exposure to large solar particle events in space. In: Kraft, G. (Ed.), *Life Sciences and Space Research XXIV*. Pergamon Press Ltd., Oxford, pp. 339–348.
- Vastel, L., Meunier, A., Siney, H., Sedel, L., Courpied, J.-P., 2004. Effect of different sterilization processing methods on the mechanical properties of human cancellous bone allografts. *Biomaterials* 25, 2105–2110.
- Walsh, W.R., Guzelsu, N., 1994. Compressive properties of cortical bone: mineral-organic interfacial bonding. *Biomaterials* 15, 137–145.
- Walsh, W.R., Ohno, M., Guzelsu, N., 1994. Bone composite behavior: effects of mineral-organic bonding. *Journal of Materials Science Materials in Medicine* 5, 72–79.
- White, J.M., Goodis, H.E., Marshall, S.J., Marshall, G.W., 1994. Sterilization of teeth by gamma radiation. *Journal of Dental Research* 73, 1560–1567.
- Wilson, E.E., Awonusi, A., Morris, M.D., Kohn, D.H., Tecklenburg, M.M.J., Beck, L.W., 2006. Three structural roles for water in bone observed by solid-state NMR. *Biophysical Journal* 90, 3722–3731.
- Wise, E.R., Maltsev, S., Davies, M.E., Duer, M.J., Jaeger, C., Loveridge, N., Murray, R.C., Reid, D.G., 2007. The organic-mineral interface in bone is predominantly polysaccharide. *Chemistry of Materials* 19, 5055–5057.
- Young, M.L., Almer, J.D., Daymond, M.R., Haeffner, D.R., Dunand, D.C., 2007. Load partitioning between ferrite and cementite during elasto-plastic deformation of an ultrahigh-carbon steel. *Acta Materialia* 55.
- Yuan, F., Almer, J., Dunand, D.C., Brinson, L.C., 2010. A new model to simulate the elastic properties of mineralized collagen fibril. *Biomechanics and Modeling in Mechanobiology*.
- Zhang, Y., Homsy, D., Gates, K., Oakes, K., Sutherland, V., Wolfbarger Jr., L., 1994. A comprehensive study of physical parameters, biomechanical properties, and statistical correlations of iliac crest bone wedges used in spinal fusion surgery. *Spine* 19, 304–308.
- Zioupos, P., Currey, J.D., Hamer, A.J., 1999. The role of collagen in the declining mechanical properties of aging human cortical bone. *Journal of Biomedical Materials Research* 45.